INTERNATIONAL JOURNAL FOR NUMERICAL METHODS IN FLUIDS
Int. J. Numer. Meth. Fluids 2001; **37**: 297–319 (DOI: 10.1002/fld.172)

Large eddy simulation of turbulent flows by a least-squares finite element method

Xu Ding and Tate T.H. Tsang*,[1]

Department of Chemical Engineering and Materials Science, University of Kentucky, Lexington, KY, U.S.A.

SUMMARY

The least-squares finite element method (LSFEM) based on first-order formulations of governing equations has been used successfully for incompressible and compressible flows and transport processes. It has not been applied to turbulent flows. In this work, large eddy simulation (LES) with dynamic subgrid-scale models is used to simulate turbulent flows. The LSFEM is implemented to solve the filtered LES equations for turbulent flows and transport processes. Numerical experiments have been carried out for three types of turbulent flows, turbulent channel flow, transitional recirculating flow, and thermal convective turbulent flow. Numerical results are compared with experimental data or direct numerical simulation results. Copyright © 2001 John Wiley & Sons, Ltd.

KEY WORDS: large eddy simulation; least-squares finite element method; turbulent flows

1. INTRODUCTION

Large eddy simulation (LES) is an effective method to simulate complex turbulent flows by resolving only the large scales of motion and modeling the subgrid scales. Its complexity and computational requirements are between direct numerical simulation (DNS) and Reynolds-averaged Navier–Stokes (RANS). Finite difference, finite volume and spectral methods are commonly used in LES. Explicit or semi-implicit time-integration schemes together with projection methods for the filtered Navier–Stokes equations have found numerous applications in LES of turbulent flows.

Finite element methods are more amenable to flow problems with complicated geometry domain and various types of boundary conditions. However, they have been not commonly used in LES of turbulent flows. The main challenge is to obtain numerical solutions for the large linear system in an efficient manner. For time-dependent, three-dimensional flow problems, the linear system of equations is large and sparse and its numerical solutions by

* Correspondence to: Department of Chemical Engineering and Materials Science, University of Kentucky, Lexington, KY 40508-0046, U.S.A.
[1] E-mail: tsang@engr.uky.edu

Received 31 May 2000
Revised 16 December 2000

direct methods lead to prohibitively large memory requirements and computing time. Thus, iterative methods become viable alternatives.

The least-squares finite element method (LSFEM) leads to symmetric positive definite linear systems for which preconditioned conjugate gradient methods can provide efficient iterative solutions. Jiang *et al*. [1], Jiang [2], and Tang [3] used the Jacobi conjugate gradient method and a matrix-free approach to simulate three-dimensional incompressible flows. They have shown that such an approach leads to a relatively efficient iterative solver with much less memory requirement. Our current iterative solvers only require four global vectors as working space [4]. We have used this approach to solve three-dimensional flow problems with more than 7 million unknowns on a single processor [4].

The LSFEM has been used successfully for incompressible and compressible flows and transport problems [2,5,6], but it has not been applied to the simulation of turbulent flows. Our objective in this work is to apply the LSFEM to carry out large eddy simulation of turbulent flows. In these simulations, small scales of motions will be modeled by subgrid-scale (SGS) models. The model coefficient(s) will be dynamically determined. The dynamic SGS models allow energy back-scattering from the small scales to large scales and result in correct asymptotic flow behavior near a solid wall.

The paper is organized as follows. In Sections 2 and 3, we briefly outline the governing equations for LES and show how to implement the SGS models for isothermal turbulent shear flows and for thermal convective turbulent flows. In Section 4, we briefly mention the numerical approaches adopted in the LSFEM/LES code, and in Section 5, we provide the LES results on three case studies: LES of a lid-driven cavity flow, LES of a turbulent channel flow, and LES of thermal turbulent flows. A summary and conclusions are given in Section 6.

2. GOVERNING EQUATIONS FOR LES

The governing equations of an incompressible flow and transport process may be written in a Eulerian reference frame as follows:

$$\frac{\partial u_j}{\partial x_j} = 0 \tag{1}$$

$$\frac{\partial u_i}{\partial t} + \frac{\partial (u_i u_j)}{\partial x_j} = \frac{1}{\rho}\frac{\partial p}{\partial x_i} + \frac{\partial}{\partial x_j}\left(\nu\left(\frac{\partial u_i}{\partial x_j} + \frac{\partial u_j}{\partial x_i}\right)\right) + f_i \tag{2}$$

$$\frac{\partial \Phi}{\partial t} + \frac{\partial (u_j \Phi)}{\partial x_j} = \frac{\partial}{\partial x_j}\left(\alpha \frac{\partial \Phi}{\partial x_j}\right) + \phi_s \tag{3}$$

where u_i is the velocity component, p the pressure, ρ the fluid density, ν the kinematic viscosity, and f_i is the body force per unit mass. Φ is any scalar quantity such as species concentration or temperature. ϕ_s is the source term of the scalar quantity. α is the diffusivity of the scalar quantity.

According to the general approach described by Leonard [7], the large scale components of LES are actually the result of applying a filtering procedure to the local and instantaneous quantities

$$\bar{f}(\vec{\mathbf{x}}, t) = \int f(\vec{\mathbf{x}}', t) G(\vec{\mathbf{x}}, \vec{\mathbf{x}}')\, \mathrm{d}\vec{\mathbf{x}}' \tag{4}$$

where f is any scalar or vectorial quantity, and G is a normalized weighting function or filter. In practical applications, the filter function is often rewritten in the component form

$$\bar{f}(x_1, x_2, x_3, t) = \int f(x_1', x_2', x_3', t) \prod_{i=1}^{3} G_i(x_i, x_i')\, \mathrm{d}x_1'\, \mathrm{d}x_2'\, \mathrm{d}x_3' \tag{5}$$

where G_i is the filter function in the i-direction. Gaussian filter function, 'top-hat' filter function and sharp-cutoff filter function are commonly used in LES.

Applying the filtering procedure to the governing equations yields additional terms $\overline{u_i u_j} - \bar{u}_i \bar{u}_j$ and $\overline{u_j \Phi} - \bar{u}_j \bar{\Phi}$; which are respectively referred to as the SGS stress tensor (denoted by τ_{ij}) and scalar fluxes (denoted by φ_j). Most SGS models use an eddy viscosity approach to model the SGS tensor and an eddy diffusivity approach to model the SGS flux, i.e.

$$\tau_{ij} = \frac{1}{2} \tau_{kk} \delta_{ij} - 2 \nu_t \bar{S}_{ij} \tag{6}$$

and

$$\varphi_j = -\alpha_t \frac{\partial \bar{\Phi}}{\partial x_j} \tag{7}$$

where

$$\bar{S}_{ij} = \frac{1}{2} \left(\frac{\partial \bar{u}_i}{\partial x_j} + \frac{\partial \bar{u}_j}{\partial x_i} \right) \tag{8}$$

ν_t and α_t are eddy viscosity and eddy diffusivity respectively. By introducing a modified pressure

$$\bar{P} = \bar{p} + \frac{1}{3} \tau_{kk} \tag{9}$$

we can obtain LES equations for incompressible turbulent flows and transport processes as

$$\frac{\partial \bar{u}_j}{\partial x_j} = 0 \tag{10}$$

$$\frac{\partial \bar{u}_i}{\partial t} + \frac{\partial (\bar{u}_i \bar{u}_j)}{\partial x_j} = -\frac{1}{\rho}\frac{\partial \bar{P}}{\partial x_i} + 2\frac{\partial}{\partial x_j}((\nu + \nu_t)\bar{S}_{ij}) + \bar{f}_i \tag{11}$$

and

$$\frac{\partial \bar{\Phi}}{\partial t} + \frac{\partial (\bar{u}_j \bar{\Phi})}{\partial x_j} = \frac{\partial}{\partial x_j}\left((\alpha + \alpha_t)\frac{\partial \bar{\Phi}}{\partial x_j}\right) + \bar{\phi}_s \tag{12}$$

The eddy viscosity ν_t and eddy diffusivity α_t require specification in simulations.

3. SGS MODELS

The most widely used SGS model for ν_t is the Smagorinsky model [8]. By assuming equilibrium between energy transfer from large scales to small scales and energy dissipation by the latter, Smagorinsky derived the eddy viscosity as

$$\nu_t = (C_s \Delta)^2 |\bar{S}| \tag{13}$$

in which $|\bar{S}|$ is the norm of large scale strain rate tensor, and C_s is referred to as the Smagorinsky constant. Δ is the grid size. For anisotropic grids, the cubic root of the cell volume, $\Delta = (\Delta_1 \Delta_2 \Delta_3)^{1/3}$, is usually employed. When the model coefficient C_s is taken a constant, its determination is generally based on the analysis of DNS data, experimental results, or some turbulence statistical theories. In general, LES results obtained from *a priori* prescription of the model coefficient can hardly match the results of transitional flows and non-equilibrium turbulent flows. To overcome this difficulty, a dynamical approach to determine the model coefficient has been proposed by Germano *et al*. [9]. The basic philosophy of the approach is to calculate the coefficients based on the smallest resolved scales. This procedure is accomplished by introducing a test filter with a filter width larger than that of the basic grid filter and by establishing a quantitative relation between the two filters. The dynamical approach has been applied to the Smagorinsky model, mixed model, and one-equation model to form the corresponding dynamical models. In the following, we will illustrate the dynamical procedure based on the Smagorinsky model.

In order to calculate the model coefficient, Germano *et al*. [9] introduced a *test filter* (denoted by a tilde) with a larger characteristic length based on the basic averaging filter. Applying the test filter to the LES formulation yields the test grid-scale stress

$$T_{ij} = \widetilde{\bar{u}_i \bar{u}_j} - \tilde{\bar{u}}_i \tilde{\bar{u}}_j \tag{14}$$

The relationship between the turbulent stresses on the two fields is as follows:

$$T_{ij} - \tilde{\tau}_{ij} = L_{ij} \tag{15}$$

where

$$L_{ij} = \widetilde{\bar{u}_i \bar{u}_j} - \tilde{\bar{u}}_i \tilde{\bar{u}}_j \tag{16}$$

Although L_{ij} can be explicitly evaluated, T_{ij} and $\tilde{\tau}_{ij}$ have to be modeled. If the Smagorinsky model is applied to both filters, we will have

$$\tilde{\tau}_{ij} - \frac{1}{3}\tilde{\tau}_{kk}\delta_{ij} = -2c\Delta^2 \widetilde{|\bar{S}|\bar{S}}_{ij} \tag{17}$$

and

$$T_{ij} - \frac{1}{3}T_{kk}\delta_{ij} = -2c\tilde{\Delta}^2 |\tilde{\bar{S}}|\tilde{\bar{S}}_{ij} \tag{18}$$

where $c = C_s^2$ and $\tilde{\Delta}$ is the characteristic length of the test filter. The derivation of Equation (18) is based on the assumption that variation of c is small in the test filter. Substituting Equations (17) and (18) into Equation (15), we have

$$L_{ij} - \frac{1}{3}L_{kk}\delta_{ij} = -2cM_{ij} \tag{19}$$

where

$$M_{ij} = \beta^2 \Delta^2 |\tilde{\bar{S}}|\tilde{\bar{S}}_{ij} - \Delta^2 \widetilde{|\bar{S}|\bar{S}}_{ij} \tag{20}$$

where

$$\beta = \frac{\tilde{\Delta}}{\Delta}$$

Using the least-squares approach, Lilly [10] obtained the model coefficient

$$c = -\frac{1}{2}\frac{L_{ij}M_{ij}}{M_{ij}M_{ij}} \tag{21}$$

Thus, the model coefficient is determined based on resolved fields. It is a function of time and space. Because the coefficient can be negative, it implies that the model can allow the back-scatter of energy from small scales to large scales.

For transport processes, it is required to solve Equations (10)–(12) and to model both the eddy viscosity ν_t and the eddy diffusivity α_t. If the momentum Equation (11) is decoupled from the scalar transport equation (12), the above dynamical procedure can be used to determine ν_t and α_t independently [11]. However, this procedure will become more complicated when the momentum equation is coupled with the transport equation. For instance, the eddy viscosity and the eddy diffusivity for turbulent thermal convection can be written in the modified Smagorinsky model as follows:

$$\nu_t = (C\Delta)^2\left(|\bar{S}|^2 - \frac{1}{Pr_t}\frac{\partial\theta}{\partial x_2}\right)^{1/2} \tag{22}$$

$$\alpha_t = \frac{(C\Delta)_2}{Pr_t}\left(|\bar{S}|^2 - \frac{1}{Pr_t}\frac{\partial\theta}{\partial x_2}\right)^{1/2} \tag{23}$$

Here, θ is temperature. When using a dynamical procedure to solve the coupled unknown coefficients, an iteration procedure is required in each step [12]. Instead of using Equations (22) and (23), Wong and Lilly [13] applied a dynamical procedure to the following equations:

$$\nu_t = C^{4/3}\Delta^{4/3}\epsilon^{1/3} \tag{24}$$

$$\alpha_t = \frac{C^{4/3}}{Pr_t}\Delta^{4/3}\epsilon^{1/3} \tag{25}$$

They introduce a new model coefficient as

$$C_\epsilon = C^{4/3}\epsilon^{1/3} \tag{26}$$

based on the assumption that the dissipative rate ϵ, and therefore C_ϵ, is insensitive to the grid filter which because the intermittency effect on ϵ is small [14]. Thus, it is possible to determine independently the two model coefficients. This approach will be used in our case study of turbulent thermal convection.

Using the dynamical procedure to determine model coefficient(s) may possibly result in computational instability due to large negative values. In order to overcome this difficulty, some kinds of averaging procedures are generally implemented. In many applications, the computation is stabilized by averaging the relevant equations over statistically homogeneous directions. This approach is simple and effective for homogeneous flows, but it is not applicable to inhomogeneous flows in complex geometry. For such cases, two general averaging procedures, spatial averaging [15] and Lagrangian averaging [16] have been proposed. In spatial averaging, the model coefficient is dynamically determined by solving an intergral equation over the entire domain. The averaging over homogeneous directions can be considered as a special case of spatial averaging. In Lagrangian averaging, the averaging procedure is taken over pathlines. The model coefficient can be dynamically computed by solving two relaxation–transport equations.

4. NUMERICAL ASPECTS

For time-dependent non-linear LES equations, we will use the Crank–Nicolson method for time integration, and Newton iteration for linearization of the non-linear convection terms. The LSFEM is used for spatial discretization. The resulting linear system of equations will be solved by a Jacobi preconditioned conjugate gradients method. The reason for selecting diagonal entries as preconditioners is that we can develop an element-to-element approach.

Thus, no global matrix or even element matrices are required for storage. This approach dramatically reduces the memory requirement for three-dimensional flow problems.

The LSFEM is developed in first-order forms of partial differential equations. The governing equations can be written in different first-order forms, such as velocity–vorticity–pressure or velocity–stress–pressure. So far, the velocity–vorticity–pressure formulation has been successfully applied to most numerical studies on several three-dimensional flows and transport processes [1,2,17,5]. The details of the LSFEM formulation have been addressed in these publications and will not be repeated here. The velocity–stress–pressure formulation is generally limited to simple two-dimensional model problems or is used for mathematical analysis [18]. Although the velocity–stress–pressure formulation leads to more unknowns, Ding [4] carried out numerous simulations and proved that the formulation provides good convergence rate and accuracy for the resulting symmetric, positive definite linear system of equations. Additionally, stress is also an important quantity in the study of turbulence. Thus, we use velocity–stress–pressure form in our LES of turbulent flows. For Rayleigh–Benard convection problems, Tang and Tsang [5] solved coupled momentum equations and the transport equation. They used a velocity–vorticity–pressure–temperature–heat flux formulation. This system includes 12 equations and 11 variables. To avoid solving larger linear systems, we decouple the governing equations, and solve independently the momentum equation and the energy balance equation. The buoyancy term in the momentum equation is explicitly computed by the Taylor series with the use of the energy balance equation [4]. This approach requires less storage and CPU time than the approach by solving the coupled equations because the work space for solving momentum equations can be used for solving energy equations. The results are in good agreement with those obtained by solving the coupled equations.

5. NUMERICAL EXPERIMENTS

5.1. LES of recirculating flow

Our first case study for the application of LES is to simulate three-dimensional lid-driven cavity flows at a Reynolds number of 3200. The flow at this Reynolds number is basically laminar but exhibits relatively unstable and low-frequency fluctuations due to the formation of Taylor–Görtler-like vortices. We will work on the domain with the aspect ratio (1:1:1). The domain is first meshed with $50 \times 50 \times 50$ trilinear elements. In order to handle large velocity gradients near the walls, we refine the three-layer grids near the wall so that we have $60 \times 60 \times 60$ elements with the minimum size of 0.005 and the maximum size of 0.02. The simulation started from the static state (impulsively started simulation) using $Re = 400$ without calling the subroutine for the dynamic SGS model over 5 dimensionless time units. The computed result was used as our initial field of LES for $Re = 3200$. The time step is set as 0.1 dimensionless time units. The simulation continues over 200 dimensionless time units and then statistics were collected over an additional 50 time units.

Figure 1 displays the time-averaging mean velocities $\langle \bar{u} \rangle$ and $\langle \bar{v} \rangle$, the root-mean-square (r.m.s.) velocities $\sigma(u'')$ and $\sigma(v'')$, and the Reynolds stress $\langle u''v'' \rangle$ at the centerlines on the mid-plane. Here the fluctuations u_i'' are defined as

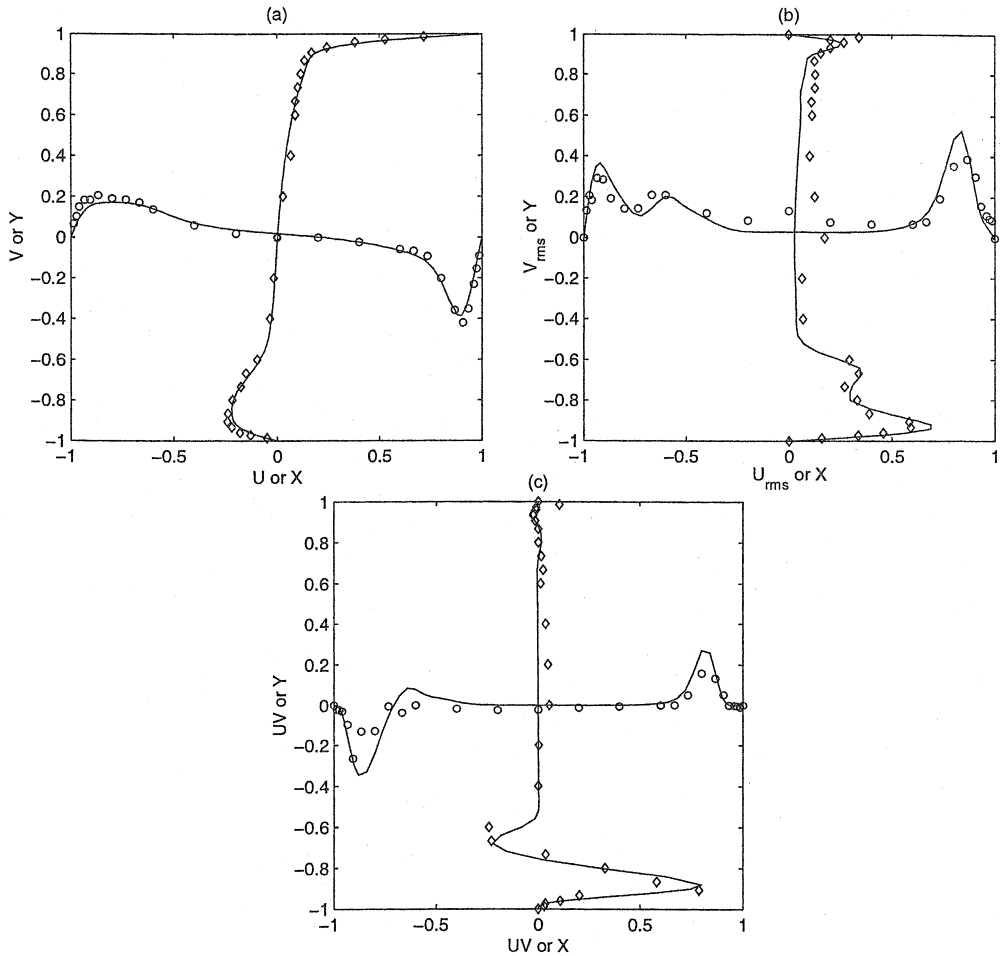

Figure 1. Quantities at the centerlines on the midplane for $Re = 3200$. ○ and ◇, Prasad and Koseff [19]; —, present results. (a) Dimensionless mean velocities: $U = \langle \bar{u} \rangle$, $V = \langle \bar{v} \rangle$; (b) The r.m.s. velocities: $U_{\text{r.m.s.}} = 10\sigma(u'')$, $V_{\text{r.m.s.}} = 10\sigma(v'')$. (c) The Reynolds stress: $UV = 500\langle u''v'' \rangle$.

$$u_i'' = \bar{u}_i - \langle \bar{u}_i \rangle \tag{27}$$

where $\langle\ \rangle$ denote time averaging, and the r.m.s. velocity is given by

$$\sigma(u_i'') = \sqrt{\langle u_i''^2 \rangle} \tag{28}$$

It should be mentioned that the Reynolds stresses being used here follow the conventional time averaging and are different from the SGS Reynolds stresses. In Figure 1(a), the computed

centerline velocities compare well with the experimental data by Prasad and Koseff [19], but the numerical solution slightly underestimates the maxima. The reason may be due to the use of uniform mesh near the center of the cavity. It can be observed from Figure 1(b) that the LES predicts the peaks of the r.m.s. velocity near the upstream, downstream, and the bottom walls. The LES result also agrees with the experimental results for the Reynolds stress (see Figure 1(c)). Figure 2 shows the flow patterns at three mid-planes. It is obvious that there are pairs of Taylor–Görtler-like vortices (see Figure 2(b)).

5.2. LES of channel flows

Simulations are carried out for the Reynolds number of 180, which is based on the wall-shear velocity, $u_\tau = (\tau_w/\rho)^{0.5}$ and the channel half-width δ. The flows around this Reynolds number have been studied by experiments and simulations. The computational domain used in this case study is the minimum flow unit, recommended by Jiménez and Moin [20]. The streamwise and spanwise lengths are $\pi\delta$ and $0.289\pi\delta$, roughly equal to 570 and 160 wall units ($\delta u_\tau/\nu$) respectively. The domain has been used by Choi *et al.* [21] for the simulation of the same Reynolds number flow to test their fully implicit scheme. The domain is meshed with $32 \times 64 \times 32$ trilinear elements in the x, y, and z (or x_1, x_2, and x_3) directions respectively. Uniform meshes with spacing $\Delta x^+ \approx 17.6$ and $\Delta z^+ \approx 5.11$ are used in the streamwise and spanwise directions.[2] A non-uniform mesh is used in the y or wall-normal direction. The finest mesh point away from the wall is $\Delta y^+ \approx 1.35$ and the maximum spacing at the centerline of the channel is about 13.5 wall units.

The initial flow field implements a two-dimensional mean flow with three-dimensional disturbances [22]

$$u(x, y, z) = c(1 - y^8) + \varepsilon \frac{L_x}{2} \sin(\pi y) \cos \frac{4\pi x}{L_x} \sin \frac{2\pi z}{L_z} \tag{29}$$

$$v(x, y, x) = -\varepsilon(1 + \cos(\pi y)) \sin \frac{4\pi x}{L_x} \sin \frac{2\pi z}{L_z} \tag{30}$$

$$w(x, y, x) = -\varepsilon \frac{L_z}{2} \sin \frac{4\pi x}{L_x} \sin(\pi y) \cos \frac{2\pi z}{L_z} \tag{31}$$

where L_x and L_z are the length of the computational domain in the x- and z-directions respectively, and ε is 10% of the averaged mean velocity. c is a constant, chosen to be 16. Fully developed turbulent channel flow is homogeneous in the streamwise and spanwise directions, so periodic boundary conditions are applied in these directions. In addition, no-slip conditions are set on the walls.

[2] The superscript $+$ denotes a non-dimensional quantity scaled by the wall variables: the velocity, u_τ; the length, ν/u_τ; and the time, ν/u_τ^2.

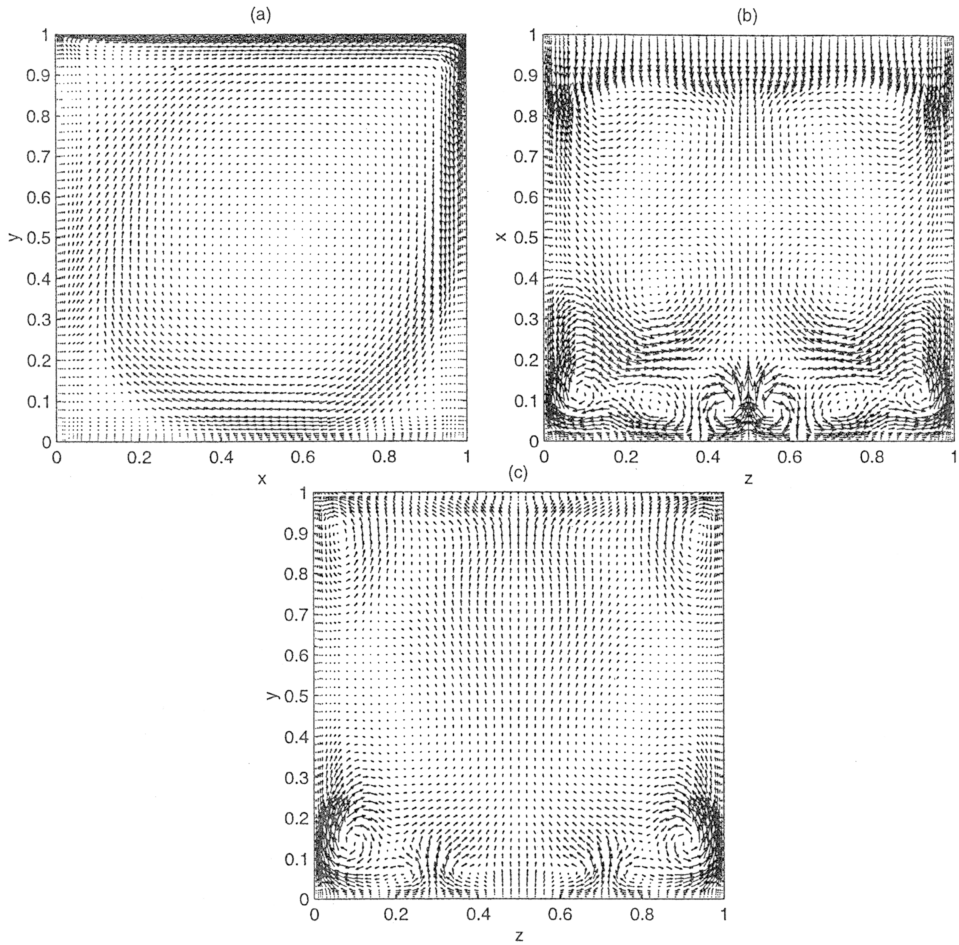

Figure 2. Velocity vector plots on mid-planes for $Re = 3200$ at time $= 250$.

The dynamical SGS model described in Section 3 is used, and the averaging is taken over the homogeneous directions. The time step is set as 1/360 time units δ/u_τ, which corresponds to $\Delta t u_\tau^2/\nu = 0.5$. Choi *et al.* [21] suggested that the time step for implicit scheme should be less than the Kolmogorov time scale ($t^+ = (u_\tau^4/\epsilon\nu)^{0.5}$) in order to maintain the simulation of turbulence (where ϵ is the dissipation rate per unit mass). The computation was carried out over about 12 time units. The statistics data were collected for a later 6 time units. The profile of the mean velocity, non-dimensionalized by the wall-shear velocity is compared with the law of the wall ($u^+ = (1/0.41) \ln y^+ + 5.20$) in Figure 3. Our numerical results are closed to the law of the wall but a little lower than the DNS results [23] near the symmetric plane. Najjar and Tafti [24] carried out a series of LES using second-order and fifth-order finite difference

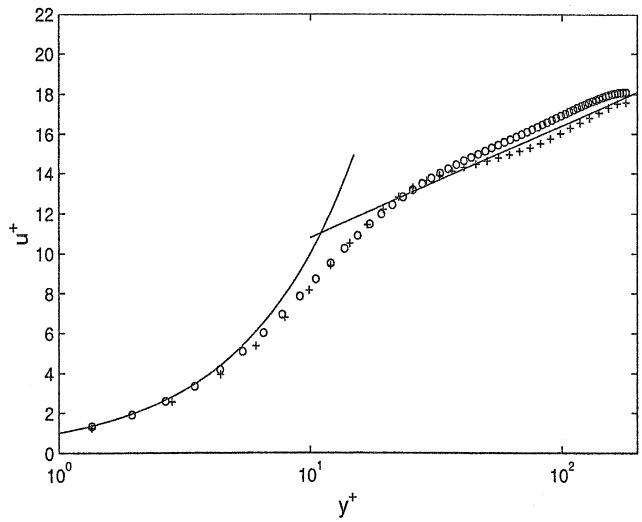

Figure 3. Mean velocity profiles in wall co-ordinates. —, law of the wall; + + +, LES/LSFEM; ○ ○ ○, DNS [23].

methods and different test filters for the same Reynolds number flow. Their results showed that a higher-order scheme predicts higher mean velocity than a lower-order scheme for the same test filtering operation. Thus, the use of trilinear elements for relatively coarse meshes near the symmetric plane is a possible reason of the underprediction of the mean velocity. The ratio of the bulk mean velocity to the central velocity is about 1.18, which is close to the DNS and the experimental results of 1.16.

In order to compare statistics, fluctuating velocities u_i'', are defined as

$$u_i'' = \bar{u}_i - \langle \bar{u}_i \rangle \tag{32}$$

where $\bar{u}_i$ is the resolved velocity and $\langle \bar{u}_i \rangle$ represents the temporal-spatial average of the velocity field. Distribution of the shear–stress in wall co-ordinates is given in Figure 4. Figure 5 displays the r.m.s. velocity fluctuations, normalized by the wall-shear velocity. Also shown are the results of the DNS data by Kim *et al.* [23] and experimental data by Kreplin and Eckelmann [25]. The fluctuations of u have shown a reasonable agreement with the DNS and the experimental data although it gives a larger maximum than others. A larger deviation from the experimental data is found near the wall for the fluctuations of v and w, but our results are more consistent with the DNS results.

Some higher-order statistical data of skewness factor and flatness factor are shown in Figures 6 and 7. The skewness factor of the fluctuation velocity field, $S(u_i'')$, is defined as

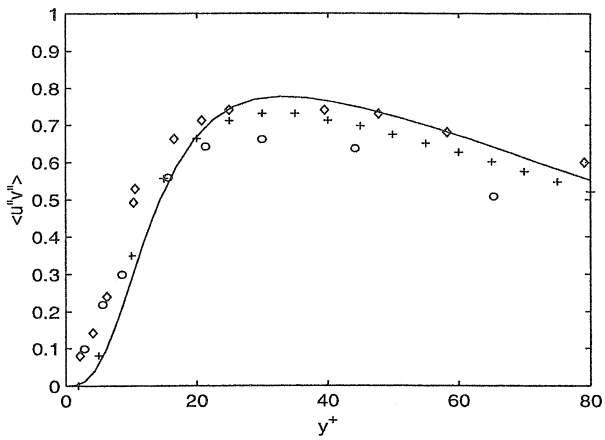

Figure 4. Reynolds shear stress normalized by the wall shear velocity. —, LES/LSFEM; + + +, DNS [23]; ○ ○ ○, experimental data for $Re_\tau = 142$ [37]; ◇ ◇ ◇, experimental data for $Re_\tau = 208$ [25].

$$S(u_i'') = \frac{\langle \bar{u}_i''^3 \rangle}{\langle \bar{u}_i''^2 \rangle^{3/2}} \tag{33}$$

and the flatness factor of the fluctuation velocity field, $F(u_i'')$, is given as

$$F(u_i'') = \frac{\langle \bar{u}_i''^4 \rangle}{\langle \bar{u}_i''^2 \rangle^2} \tag{34}$$

The calculated skewness factors are given in Figure 6 and compared with experimental data [25] and DNS results [23]. Figure 6(a) and (b) show that computing values are in favorable agreement with measurements and the DNS results except for the discrepancy near the wall. The computed $S(u'')$ is smaller than the measurements and DNS results near the wall. There are obvious differences for $S(v'')$ values near the wall. Our values have a better agreement with the recent experimental results by Niederschulte *et al.* [26], who used a laser-Doppler technique to examine the turbulent flow at $Re = 178.6$ (not shown in the figure). For $S(w'')$, experimental results and DNS results (not shown in the figure) are approximately equal to zero. It seems that our LES/LSFEM result oscillates around the zero value.

For flatness factors, the computed values also showed good agreement with experimental and DNS results away from the wall (see Figure 7). The computed $F(u'')$ shows smaller values near the wall, whereas the DNS has a good agreement with the experimental data. There is a significant discrepancy for $F(v'')$ between the numerical results and the experimental data near the wall. Recent experimental results of $F(v'')$ near the wall are about 4 [26]. Xu *et al.* [27] carried out a combined DNS and experimental study to examine the difference. They believe that it is difficult to experimentally measure kurtosis near the wall because of inadequate time

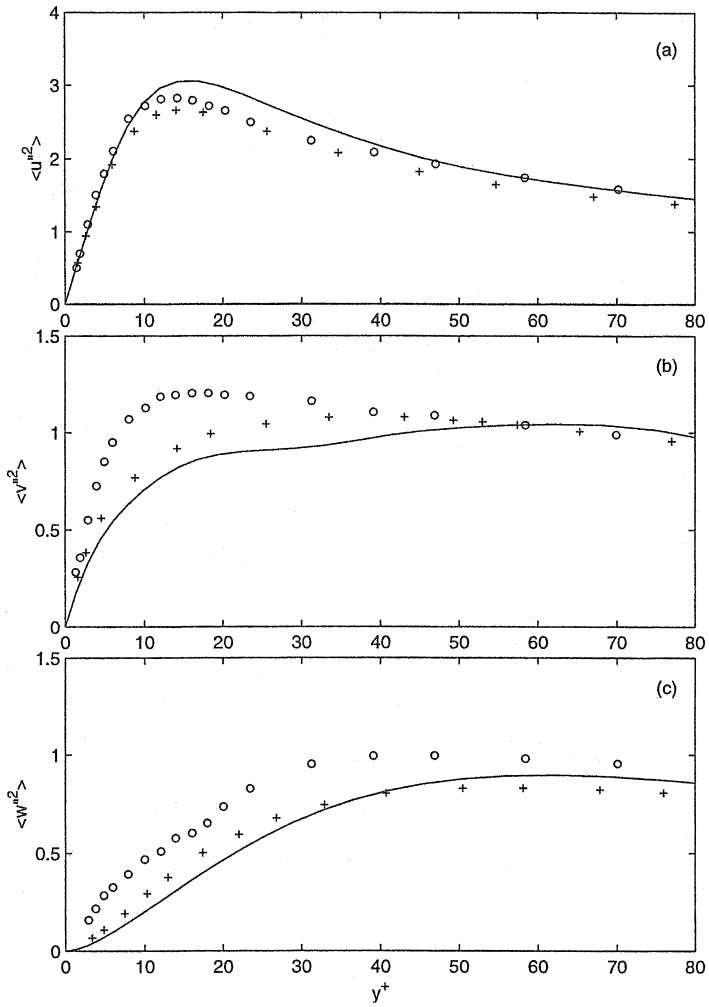

Figure 5. R.m.s. velocity fluctuations normalized by the wall shear velocity. —, LES/LSFEM; + + +, DNS [23]; ○ ○ ○, experimental data [25].

resolution, implicit filtering during data collecting and insufficient statistical accuracy. They proved indirectly that the high near-wall values of the kurtosis were physical in origin by the analysis of their DNS data. Our LES values are between the experimental values and the DNS data. Figure 7(c) shows that the computed $F(w'')$ is in excellent agreement with the experimental data and the DNS.

The average coefficient of dynamic SGS model in horizontal directions is shown in Figure 8. The result is consistent with the result for $Re_\tau = 205$ by Zhao and Voke [28].

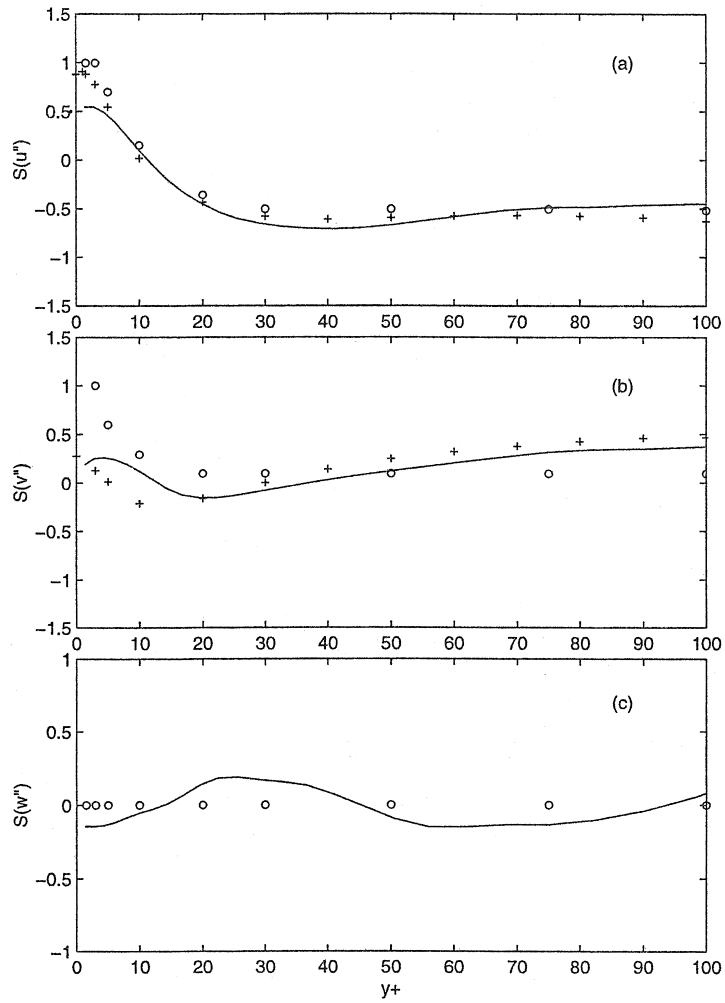

Figure 6. Skewness factors in wall co-ordinates. —, LES/LSFEM; + + +, DNS [23]; ○ ○ ○, experimental data [25].

5.3. *LES of thermal turbulent flows*

The computational domain and the co-ordinate system are shown in Figure 9. The domain is chosen by the consideration of covering the largest wavelengths. According to Deardorff and Willis [29] and Fitzjarrald [30] a minimum aspect ratio (L_1/h or L_3/h) of 3 is required for a thermal turbulent flow. In addition, a large ratio is helpful to reduce the effects of boundary conditions. The ratio is chosen as 6 in this study. The computation is carried out with 76800 trilinear elements ($40 \times 48 \times 40$, in x_1, x_2, and x_3) for Rayleigh numbers of 3.8×10^5 and

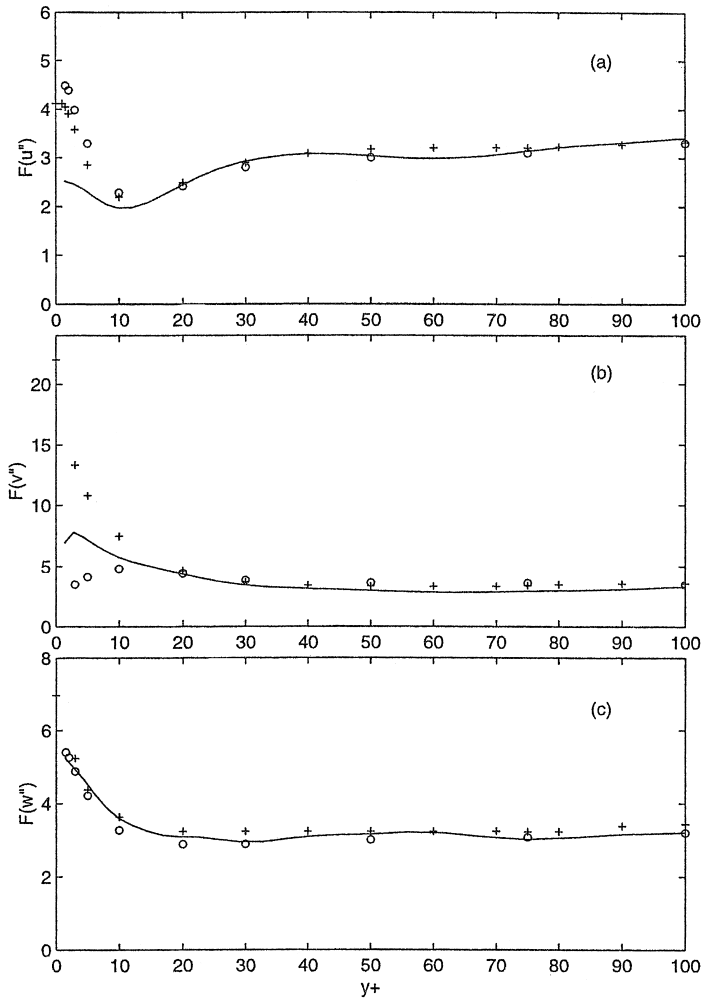

Figure 7. Flatness factors in wall co-ordinates. —, LES/LSFEM; + + +, DNS [23]; ○ ○ ○, experimental data [25].

2.5×10^6. Uniform meshes are used in horizontal directions. Non-uniform meshes are used in the vertical direction with the finest meshes near the solid walls. In order to resolve the conductive sublayer δ near the wall, it is necessary to put the first vertical grid points inside the sublayer. The sublayer thickness can be estimated by $\delta = 1/(2Nu)$, which was suggested by Goldstein and Chu [31] (where Nu is the Nusselt number).

Periodic boundary conditions are used in the horizontal directions. No-slip boundary conditions are prescribed at the top and bottom walls. The simulation starts from the state

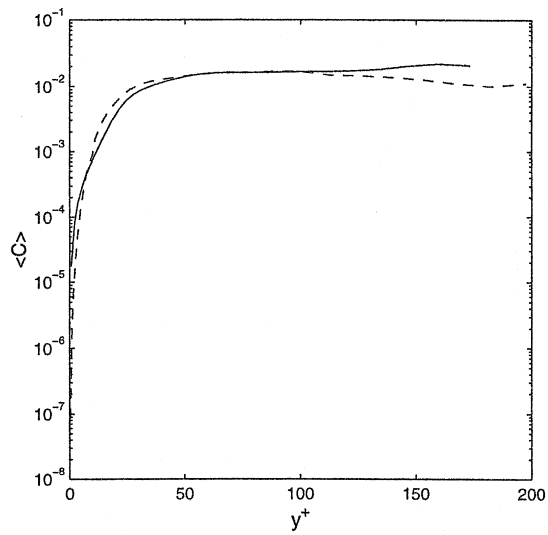

Figure 8. Mean dynamical model coefficient in wall co-ordinates. —, LES/LSFEM; – – –, Zhao and Voke [28].

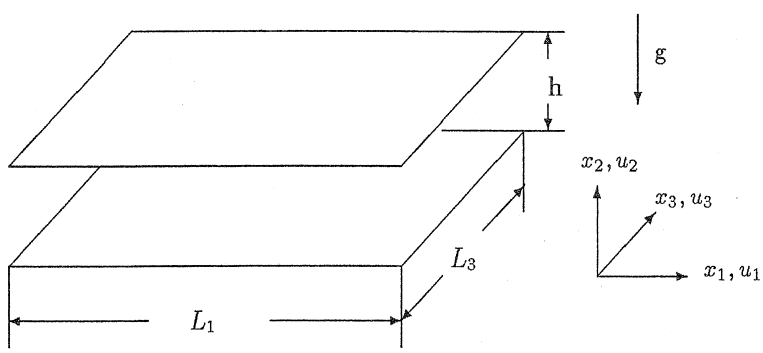

Figure 9. Computational domain and co-ordinate system for thermal turbulent flows.

with zero velocities and conduction temperature profile for Rayleigh number of 3.8×10^5. Its results are used as initial conditions for a higher Rayleigh number of 2.5×10^6.

A time step of 0.1 dimensionless time unit, $h/(g\beta h\Delta T)^{1/2}$, is used, which is larger than the values by Eidson [32]. We carry out the computations to develop a 'quasi-stationary' turbulent flow and collect the data over a longer time interval. The simulations run for 100 dimensionless time units, and then statistics are collected for additional 40 time units.

The vertical profiles of temperature averaged in horizontal directions and time are shown in Figure 10. They show good agreement with the experimental results by Deardorff and Willis [29] and the DNS data by Grotzbach [33]. The depth of the conductive sublayer decreases with increasing Rayleigh number. The profile, for a higher Rayleigh number, exhibits a larger temperature gradient near the walls, which corresponds to a higher Nusselt number. The Nusselt number is calculated as

$$Nu = \frac{\partial \bar{\theta}}{\partial x_2} + (RaPr)^{1/2} \langle \overline{u_2 \theta} \rangle \tag{35}$$

and

$$\langle \overline{u_2 \theta} \rangle = \langle \bar{u}_2 \bar{\theta} \rangle + \langle \overline{u_2 \theta} - \bar{u}_2 \bar{\theta} \rangle \tag{36}$$

where $\langle\ \rangle$ indicate time and horizontal averaging. $\langle \overline{u_2 \theta} - \bar{u}_2 \bar{\theta} \rangle$ can be estimated from the SGS model. For the Rayleigh number of 3.8×10^5, the Nusselt numbers are 6.14 and 6.04 at the bottom and upper wall respectively. For the Rayleigh number of 2.5×10^6, the two values are 10.42 and 10.19 respectively. The averaged Nusselt numbers in vertical direction are 6.2 and 10.4 respectively.

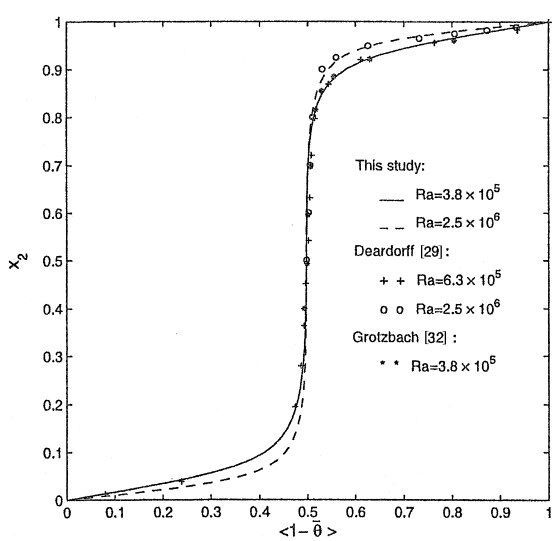

Figure 10. Horizontally averaged temperature profiles.

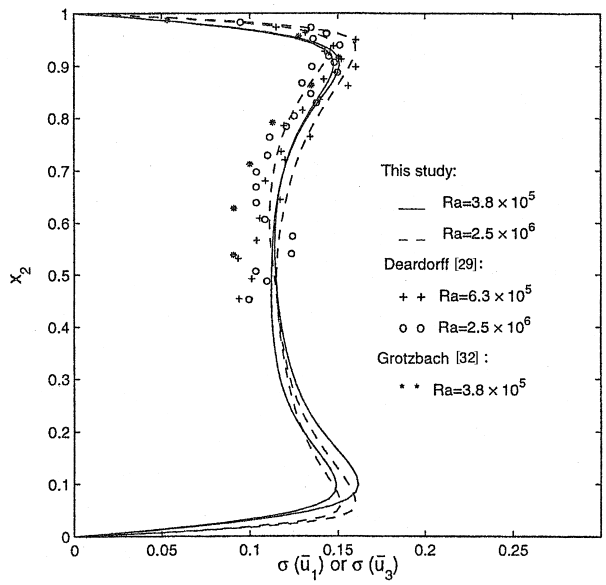

Figure 11. R.m.s. of the horizontal velocity components.

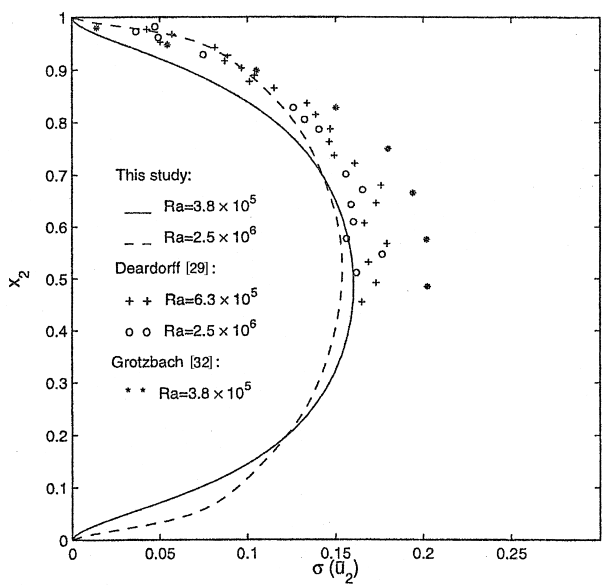

Figure 12. R.m.s. of the vertical velocity component.

In order to compare the turbulence statistics with experimental data, we follow the usual definition of the r.m.s.

$$\sigma(\phi) = \langle \phi''^2 \rangle^{1/2} = \langle (\phi - \langle \phi \rangle)^2 \rangle^{1/2} \tag{37}$$

where ϕ is the scalar quantity such as temperature or velocity components. The vertical profiles of $\sigma(u_1)$, and $\sigma(\theta)$ are shown in Figures 11–13. The numerical results compare reasonably well with the experimental data. Figure 11 also shows the vertical profiles of $\sigma(u_3)$, which do not collapse with those of $\sigma(u_1)$. This fact indicates the flows are unsymmetric in horizontal directions of x_1–x_3 plane, which is consistent with Eidson's results [32]. Because of the presence of solid walls, $\sigma(u_2)$ shows a gradual increase from zero at the wall to a maximum at the center plane. However, $\sigma(\theta)$, $\sigma(u_1)$, and $\sigma(u_3)$ show their maxima near the walls. Deardorff and Willis [29] ascribed this phenomenon to the horizontal 'mushrooming' of warm air converted upward from interior region. Our simulations realize the 'mushrooming' flows (see Figure 14). Their explanation should be understood for the region near the upper wall. Figure 14 gives the flow patterns and the contour plots of the velocity at different horizontal cross sections. Near the upper wall (Figure 14(b) and (d)), the flow in horizontal directions looks like radiation from some 'sources'. The positions of these 'sources' are approximately located where there are strong upward (positive) vertical velocity. The updrafts drive the fluid to flow in all horizontal directions because of the presence of a solid wall, where the vertical velocity becomes zero. The flows in this region are like 'mushrooming', as Deardorff and Willis described. Near the lower wall, the 'mushrooming' flows are downdrafts rather than upward

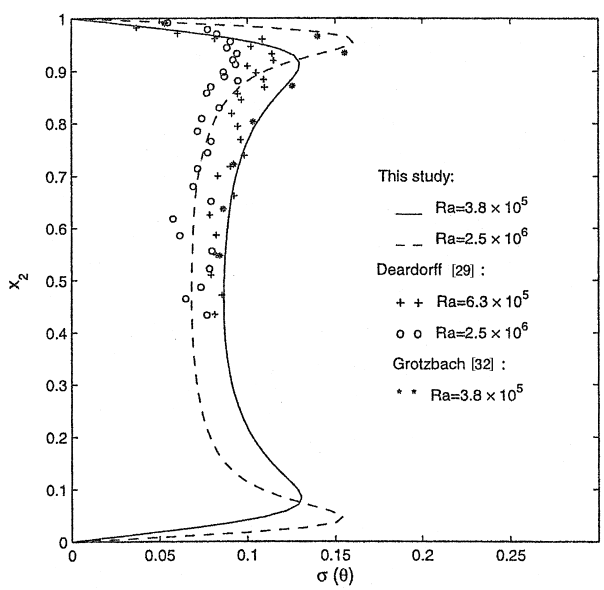

Figure 13. R.m.s. of temperature.

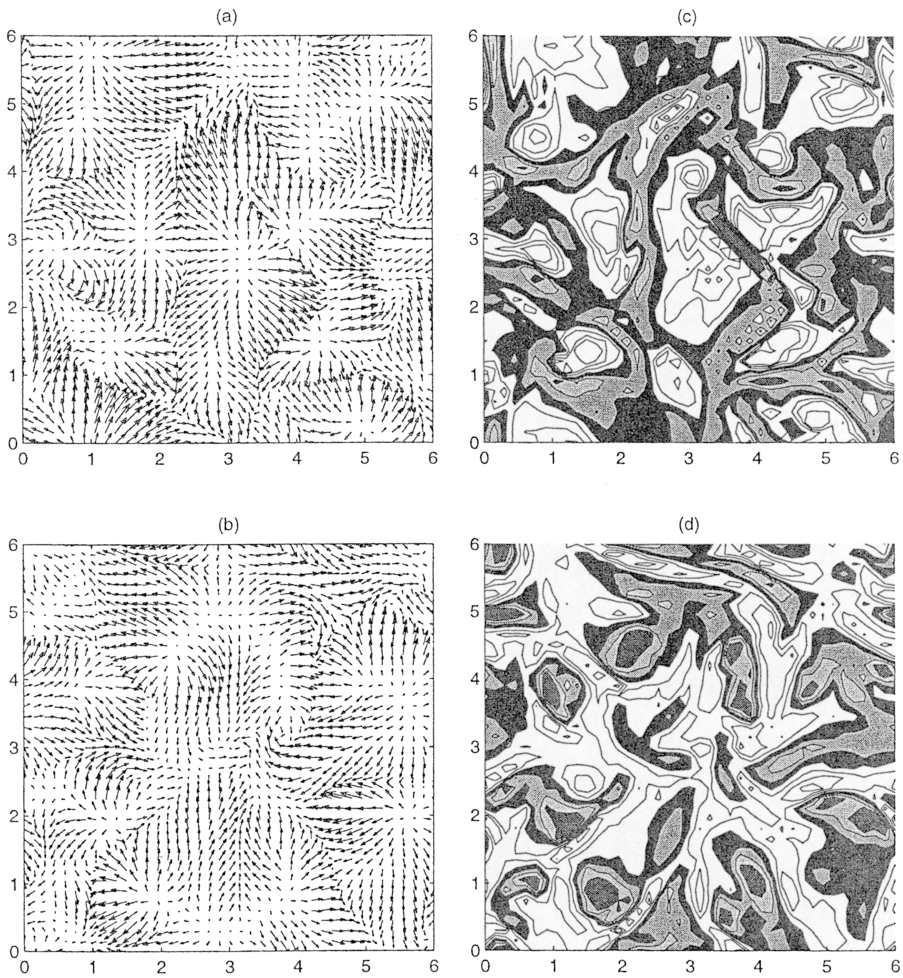

Figure 14. (a) and (b) The horizontal flow pattern near the walls ($x_2 = 0.098$ and 0.902). (c) and (d) The counter plots of the vertical velocity at the corresponding heights. $Ra = 3.8 \times 10^5$. Solid lines represent $u_2 < 0$ and filled lines represent $u_2 > 0$.

motion (see Figure 14(a) and (c)). The figures show that the positions of the 'sources' are approximately the same as those of the strong downward (negative) vertical velocity. Figure 15 plots the turbulent Prandtl number Pr_t computed by the dynamic SGS model. Near the walls, maxima exist for both cases. It is interesting to point out that the average values along the vertical directions are approximately the same (0.391 and 0.393). The values are very close to the value selected by Eidson [32], who carried out simulations with a constant model coefficient of 0.4. Works by Grotzbach [34], Grotzbach and Schumann [35], and Deardorff [36] suggested that the turbulent Prandtl number is in the range of $\frac{1}{3}$–$\frac{1}{2}$.

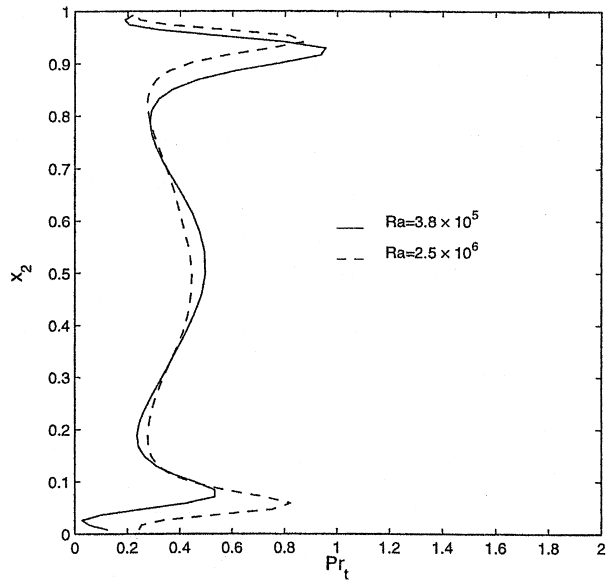

Figure 15. Vertical profiles of average turbulent Prandtl number.

6. SUMMARY AND CONCLUSIONS

The LSFEM has been used for the LES of turbulent flows. Grid resolution, as pointed out by Eidson [32], is the main issue in LES. The boundary region near the wall can be solved either by the brute force approach (using more refined meshes) or by a wall function. The less memory requirement of our LSFEM makes it possible to use fine meshes near the wall. The overall results for three case studies compare well with the experimental data or DNS results. They confirm that the LSFEM is an effective numerical method to simulate turbulent flows and transport processes. The combination of LSFEM and LES is a useful technique to simulate flows because it does not have any tuning parameter for the LSFEM nor does it require the 'a priori' prescription of turbulence model constants. Thus, the approach 'predicts' the turbulent flow behavior.

ACKNOWLEDGMENTS

This work was supported by the US Environmental Protection Agency.

REFERENCES

1. Jiang BN, Lin CY, Povinelli LA. Large-scale computation of incompressible viscous flow by least-squares finite element method. *Computer Methods in Applied Mechanics and Engineering* 1994; **114**: 213–231.
2. Jiang BN. *The Least-squares Finite Element Method.* Springer: Berlin, 1998.

3. Tang LQ. A least-squares finite element method for time-dependent fluid flows and transport phenomena. PhD dissertation, University of Kentucky, Lexington, KY, 1994.
4. Ding X. Large eddy simulation of turbulent transport processes by a least-squares finite element method. PhD dissertation, University of Kentucky, Lexington, KY, 1999.
5. Tang LQ, Tsang TTH. Temporal, spatial and thermal features of 3-D Rayleigh–Benard convection by a least-squares finite element method. *Computer Methods in Applied Mechanics and Engineering* 1997; **140**: 201–219.
6. Yu ST, Jiang BN, Wu J, Duh JC. Three-dimensional simulations of Marangoni–Benard convection in small container by the least-squares finite element method. AIAA paper 96-0863, 1996.
7. Leonard A. Energy cascade in large eddy simulation of turbulent fluid flows. *Advances in Geophysics Part A* 1974; **18**: 237–248.
8. Smagorinsky J. General circulation experiments with the primitive equations: Part I. The basic experiment. *Monthly Weather Review* 1963; **91**: 99–164.
9. Germano M, Piomelli U, Cabot WH. A dynamic subgrid-scale eddy viscosity model. *Physics of Fluids* 1991; **A3**: 1760–1765.
10. Lilly DK. A proposed modification of the Germano subgrid-scale closure method. *Physics of Fluids* 1992; **A4**: 633–635.
11. Moin P, Squires K, Cabot W, Lee S. A dynamic subgrid-scale model for compressible turbulence and scalar transport. *Physics of Fluids* 1991; **A3**: 2746–2757.
12. Sullivan P, Moeng CH. An evaluation of the dynamic subgrid scale model in buoyancy driven flows. In *Proceedings of the 10th Symposium on Turbulence and Diffusion*. AMS: Boston, MA, 1992.
13. Wong VC, Lilly DK. A comparison of two dynamic subgrid closure methods for turbulent thermal convection. *Physics of Fluids* 1994; **6**: 1016–1023.
14. Kuznetsov VR, Praskovsky AA, Sabelnikov VA. Fine-scale turbulent structure of intermittent shear flows. *Journal of Fluid Mechanics* 1992; **243**: 595.
15. Ghosal S, Moin P. The basic equations for the large eddy simulation of turbulent flows in complex geometry. *Journal of Computational Physics* 1995; **118**: 24–37.
16. Meneveau C, Lund TS, Cabot WH. A Lagrangian dynamic subgrid-scale of turbulence. *Journal of Fluid Mechanics* 1996; **319**: 353–385.
17. Tang LQ, Chang TW, Tsang TTH. Transient solutions for three-dimensional lid–driven cavity flows by a least-squares finite element method. *International Journal for Numerical Methods in Fluids* 1995; **21**: 413–432.
18. Bochev PB, Gunzburger M. Least-squares methods for the velocity–pressure–stress formulation of the Stokes equations. *Computer Methods in Applied Mechanics and Engineering* 1995; **126**: 267–287.
19. Prasad AK, Koseff JR. Reynolds number and end-wall effects on a lid-driven cavity flow. *Physics of Fluids* 1989; **A1**: 208–218.
20. Jiménez J, Moin P. The minimal flow unit in near-wall turbulence. *Journal of Fluid Mechanics* 1991; **225**: 213–240.
21. Choi H, Moin P, Kim J. Effects of the computational time step on numerical solutions of turbulent flow. *Journal of Computational Physics* 1994; **113**: 1–4.
22. Moin P, Kim J. On the numerical solution of time-dependent viscous incompressible fluid flows involving solid boundaries. *Journal of Computational Physics* 1980; **35**: 381–392.
23. Kim J, Moin P, Moser R. Turbulence statistics in fully developed channel flow at low Reynolds number. *Journal of Fluid Mechanics* 1987; **177**: 133–166.
24. Najjar FM, Tafti DK. Study of discrete test filters and finite difference approximations for the dynamic subgrid-scale stress model. *Physics of Fluids* 1996; **8**: 1076–1088.
25. Kreplin H, Eckelmann H. Behavior of the three fluctuating velocity components in the wall region of a turbulent channel flow. *Physics of Fluids* 1979; **22**: 1233–1239.
26. Niederschulte MA, Adrian RJ, Hanratty TJ. Measurement of turbulent flow in a channel at low Reynolds number. *Experimental Fluids* 1990; **9**: 222–230.
27. Xu C, Zhang Z, den Toonder JMJ, Nieuwstadt FTM. Origin of high kurtosis levels in the viscous sublayer. Direct numerical simulation and experiment. *Physics of Fluids* 1996; **8**: 1938–1944.
28. Zhao H, Voke PR. A dynamic subgrid-scale model for low-Reynolds-number channel flow. *International Journal for Numerical Methods in Fluids* 1996; **23**: 19–27.
29. Deardorff JW, Willis GE. Investigation of turbulent thermal convection between horizontal plates. *Journal of Fluid Mechanics* 1967; **28**: 675–704.
30. Fitzjarrald DE. An experimental study of turbulent convection in air. *Journal of Fluid Mechanics* 1976; **73**: 693–719.
31. Goldstein RJ, Chu TY. Thermal convection in a horizontal layer of air. *Progress in Heat Transfer* 1969; **2**: 55.
32. Eidson TM. Numerical simulation of the turbulent Rayleigh–Benard problem using subgrid modelling. *Journal of Fluid Mechanics* 1985; **158**: 245–268.

33. Grotzbach G. Direct numerical simulation of laminar and turbulent Benard-convection. *Journal of Fluid Mechanics* 1982; **119**: 27–53.
34. Grotzbach G. Numerical simulation of turbulent temperature fluctuations in liquid metals. *International Journal of Heat Mass Transfer* 1980; **24**: 475.
35. Grotzbach G, Schumann U. Direct numerical simulation of turbulent velocity-, pressure- and temperature-fields in channel flows. In *Turbulent Shear Flows I*, Durst F, *et al*. (eds). Springer: Berlin, 1979; 370–385.
36. Deardorff JW. On the magnitude of the subgrid scale eddy coefficient. *Journal of Computational Physics* 1971; **1**: 120–133.
37. Eckelmann H. The structure of the viscous sublayer and the adjacent wall region in a turbulent channel flow. *Journal of Fluid Mechanics* 1974; **65**: 439–459.

